JAAS

ROYAL SOCIETY OF CHEMISTRY

PAPER

View Article Online
View Journal

Cite this: DOI: 10.1039/d5ja00167f

Assessment of matrix effects in boron isotope analysis using 257 nm fs-LA and 193 nm ns-LA-MC-ICP-MS with new tourmaline reference materials†

Xiaojuan Nie, Yan Zhang,* Zhian Bao, Kaiyun Chen, Wenqiang Yang and Honglin Yuan*

This study compared boron (B) isotopic compositions of six chemically diverse tourmalines (including schorl, dravite, and elbaite types) using 257 nm femtosecond (fs) and 193 nm nanosecond (ns) laser ablation coupled with multi-collector inductively coupled plasma mass spectrometry (LA-MC-ICP-MS). Significant matrix effects were observed when non-matrix-matched standards were used, leading to δ^{11}B deviations of −0.70‰ to −0.41‰ for fs-LA and −0.63‰ to −0.57‰ for ns-LA when using dravite GIGT as a bracketing standard for schorl (TOUR1 and TOUR4) and elbaite (TOUR6). In contrast, using GIGT as the matrix-matched bracketing standard in the B analysis of dravites (TOUR2, TOUR3, and TOUR5) yielded significantly lower deviations of −0.22‰ to −0.18‰ for fs-LA and −0.44‰ to 0.12‰ for ns-LA. These findings necessitate matrix-matched standards for precise and accurate *in situ* measurements of B isotopes. We characterized four natural tourmaline reference materials (TOUR1, TOUR4, TOUR5, and TOUR6) for *in situ* B isotope analysis using LA-MC-ICP-MS and confirmed their isotopic homogeneity. The measured mean δ^{11}B values were −11.14 ± 0.40‰ (2SD, $n = 597$), −13.42 ± 0.57‰ (2SD, $n = 509$), −9.09 ± 0.60‰ (2SD, $n = 486$), and −8.57 ± 0.17‰ (2SD, $n = 164$), respectively, agreeing well with those obtained by solution nebulizer (SN)-MC-ICP-MS. Thus, schorl (TOUR1 and TOUR4), dravite (TOUR5), and elbaite (TOUR6) are recommended as candidate matrix-matched tourmaline reference materials for *in situ* B isotope determination.

Received 28th April 2025
Accepted 6th June 2025

DOI: 10.1039/d5ja00167f

rsc.li/jaas

1. Introduction

Boron (B) is a moderately volatile element with two stable isotopes, ^{10}B and ^{11}B, occurring in natural abundances of 19.9% and 80.1%, respectively. Due to the relatively light mass of boron coupled with a significant relative mass difference (~10%), the element exhibits substantial natural isotope variations in different geological reservoirs, ranging from −50‰ to +60‰.[1] Tourmaline, a borosilicate mineral, is widely distributed as an accessory phase in many crustal rocks, such as boron-rich peraluminous granites, pegmatites, sedimentary rocks, metamorphic rocks, and a variety of ore deposits. Tourmaline remains stable across a wide range of crustal conditions, with temperatures ranging from below 150 °C to above 900 °C and pressures from below 6 MPa to above 6 GPa, enabling it to equilibrate with various geological fluids.[2–4] These features make B isotopes of tourmalines powerful tracers for fluid–rock interactions during metamorphism, crucial for elucidating crust-mantle recycling mechanisms and highly effective in determining ore-forming fluid sources, magmatic-hydrothermal evolution processes, and boron cycling within subduction zones.[5–15]

Bulk analytical techniques such as solution nebulization multi-collector inductively coupled plasma mass spectrometry (SN-MC-ICP-MS)[16–20] and thermal ionization mass spectrometry (TIMS)[20–22] can achieve highly accurate and precise B isotopic compositions. Particularly positive (P)-TIMS can demonstrate an analytical precision of 0.1–0.3‰,[21,22] and MC-ICP-MS can achieve 0.25‰ (2SE) precision in foraminifera[16] or 0.34‰ (2SD) in diverse natural samples including seawater, peach leaves, loess, and plants.[18] They present inherent limitations for micro-scale geochemical investigations involving intra-mineral zoning or genetically distinct mineral phases. Furthermore, their application requires complex chemical treatment procedures and substantial sample amounts. Notably, a time-of-flight (TOF) mass spectrometer is also applied in isotope detection.[23,24] Retzmann *et al.* (2023)[24] utilized a second generation ICP-TOFMS with a micro-channel plate, enabling isotope detection at 0.14% precision for the ^{11}B/^{10}B intensity ratio.

The development of *in situ* analysis techniques such as secondary ion mass spectrometry (SIMS)[13,25–31] and laser ablation (LA)-MC-ICP-MS[32–35] has been increasingly applied to

---

State Key Laboratory of Continental Evolution and Early Life, Department of Geology, Northwest University, Xi'an 710069, China. E-mail: yhlsklcd@126.com; zhangyan@nwu.edu.cn

† Electronic supplementary information (ESI) available. See DOI: https://doi.org/10.1039/d5ja00167f

investigate various geological processes at the microscale. Despite lower precision compared to TIMS, SIMS analysis provides better spatial resolution (10–20 μm spot size), simpler sample preparation, and ultra-low sample consumption (<1 pg).[31] Early applications of SIMS for B isotope analysis relied on small-geometry instruments operating in mono-collection mode. The pioneering study by Chaustidon and Albarede[26] applied SIMS (Cameca IMS 3f) for determining δ^{11}B values in B-poor mantle lavas and meteoritic samples with a precision of 3.0‰ (2 s), establishing B isotopes as a powerful tracer of magmatic processes. The advent of large-geometry SIMS instruments marked a transformative leap in analytical performance. Marschall and Monteleone[29] achieved ±1.5‰ (2RSE) precision and accuracy for basalt glass with B concentrations as low as 1 μg g^{-1} using a Cameca IMS 1280. Büttner *et al.*[36] reported uncertainties of ∼0.8‰ (2 s) using a Cameca IMS 1280HR for single reference materials (RMs) (schorl HS#112566, dravite HS#108796, IAEA B4). However, significant matrix effects for B isotope determination in SIMS have already been found in previous studies. For example, MacGregor *et al.*[30] found non-negligible matrix-dependent mass fractions using a Cameca IMS 4f, with δ^{11}B offsets of −3.6‰ for schorl (HS#112566) and +1.6‰ for elbaite (HS#98144) relative to dravite (HS#108796). Recently, Marger *et al.*[31] observed significant instrument mass fractionation reaching 8‰ in δ^{11}B measurement across the schorl-dravite-elbaite solid solution (schorl IAEA-B-4, schorl HS#112566, dravite HS#108796, and elbaite HS#98144) during Cameca IMS 1280HR SIMS analysis, despite intermediate precision being better than 0.6‰ (2 s).

Compared with SIMS, LA-MC-ICP-MS has become an attractive tool for *in situ* B isotope analysis, owing to its operational simplicity, cost-effectiveness, and minimal matrix effects. Le Roux *et al.*[34] first conducted *in situ* B isotope ratio measurements using a 266 nm laser ablation system coupled with a VG Elemental Axiom double-focusing ICP-MS, demonstrating a precision of <1‰ (2 s) at the nanogram level for glasses. Hou *et al.*[37] achieved precisions of 1.12‰ (2 s) for low-B content standard IAEA B6 (∼200 ppm) and 0.58‰ and 0.97‰ (2 s) for high-B content standards IAEA B4 and IMR RB1, respectively, during the B isotope analysis by LA-MC-ICP-MS. Lin *et al.*[33] found that an X skimmer cone combined with a jet sample cone exhibited the highest boron sensitivity in LA-MC-ICP-MS, achieving accurate determination in low-B content samples (11–31 ppm). However, high precision and accurate B isotopic measurements remain challenging, primarily due to two factors: (1) instrumental mass fractionation (IMF), which can be calibrated using the standard-sample bracketing (SSB) method, requiring B isotopic homogeneous RMs at the microscopic scale and (2) elemental fractionation during laser ablation, aerosol transport, and ionization processes in the ICP source, which requires strict optimization of laser ablation conditions. Previous studies demonstrated that the femtosecond (fs) laser pulse significantly reduced the laser-induced fractionation effects compared to nanosecond (ns) pulses,[38–41] owing to the drastically shorter laser–matter interaction time, faster heat diffusion, and a minimized heat-affected zone. Furthermore, fs-LA generates stoichiometric aerosols and similar particle size distributions. The fs-LA-MC-ICP-MS technique can reduce the reliance on matrix-matched, well-characterized standards, which are often available for analysis of isotopes and trace elements. For example, Zheng *et al.*[40] conducted a systematic evaluation of matrix effects during Fe isotope analysis using 266 nm fs- and 193 nm ns-LA-MC-ICP-MS, revealing that fs-LA processes significantly reduce iron isotope fractionation compared to ns-LA. However, previous studies have shown that copper isotopic compositions are still affected by matrix effects, with non-matrix-matched methods using fs-LA. Lv *et al.*[42] reported that δ^{65}Cu values calibrated using non-matrix-matched standards were seriously affected by matrix effects, with a deviation of up to 1.42‰ using UV-fs-LA-MC-ICP-MS. Currently, the main tourmaline RMs for B isotope measurements include Schorl IAEA-B4, Schorl HS#112566, Elbaite HS#98144, Dravite HS#108796, IMR RB1, IMR RB2, and UNIL-T1 to UNL-T6.[31,37,43–45] Recently, scholars have developed some new standards for B isotope measurements, such as schorl MD-B66 and IM-B232; dravite HGL-3, GIGT, and XJ; and elbaite BR-DG68.[46–48]

This study assesses the matrix effects in tourmaline B isotope analysis by comparing matrix-matched and non-matrix-matched measurements using 193 nm ns-LA-MC-ICP-MS and 257 nm fs-LA-MC-ICP-MS. We propose four potential RMs—two schorl (TOUR1 and TOUR4), one dravite (TOUR5), and one elbaite (TOUR6)—for *in situ* B isotope analysis. Comprehensive homogeneity assessments confirm their sufficient B isotopic homogeneity at the micrometer scale, further supporting their use as matrix-matched standards.

2. Experimental

2.1 Sample preparation

Three types of megacryst tourmalines were purchased from suppliers in 2024. TOUR1 and TOUR4 are black columnar tourmaline crystals from the Guangxi Province, China (Fig. 1a and d). TOUR2 and TOUR5 are brownish black and brown columnar tourmaline crystals from Yunnan Province, China, separately (Fig. 1b and e). TOUR3 is black columnar tourmaline from Xinjiang Province, China (Fig. 1c). TOUR6 is green columnar tourmaline from Afghanistan (Fig. 1f). The six tourmalines (TOUR1–6) were cut into small pieces using a diamond wire cutter perpendicular to the long axis (*c*-axis) direction. A small portion of these tourmalines were mounted in epoxy resin surrounded by a PVC ring of 16 mm diameter and then polished for further B isotope analysis. Back-scattered electron (BSE) imaging revealed only few mineral inclusions (*e.g.*, zircon, apatite, pyrite, and calcite) within TOUR2 (Fig. 1h) and TOUR3 (Fig. 1i), while no inclusions were detected in the remaining tourmalines. Besides, sample powders were extracted from the target sample surface using a micro-drilling system (MSS VI, Relion Industries, USA) and measured for B isotope using SN-MC-ICP-MS to compare with the LA-MC-ICP-MS results.

2.2 EPMA major element determination

The major element compositions of tourmalines were determined using a JEOL JXA-8230 EPMA at the State Key Laboratory

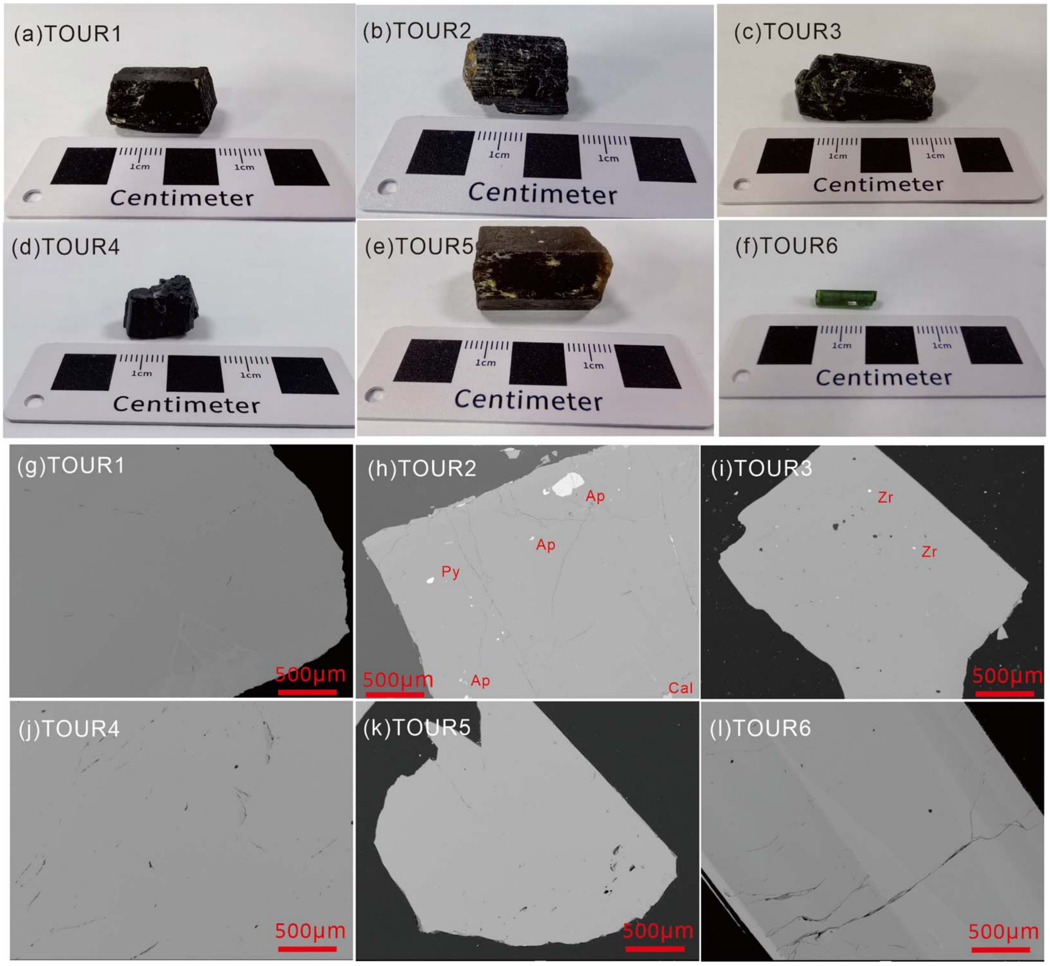

Fig. 1 Photos (a–f) and BSE images (g–l) of the six investigated tourmalines.

of Continental Evolution and Early Life (SKLCEL), Northwest University, Xi'an, China. The analytical conditions were set as 15 kV accelerating voltage, 10 nA beam current, and a 2 μm beam size. The following standards were used: olivine (Si, Mg), orthoclase (K), chromium oxide (Cr), diopside (Ca), rutile (Ti), jadeite (Na), almandine (Al), magnetite (Fe), and rhodonite (Mn).

2.3 SN-MC-ICP-MS analysis of B isotopes

NaOH alkaline fusion, ion-change chromatography, and SN-MC-ICP-MS analysis of B isotope ratios were performed at the State Key Laboratory of Palaeobiology and Stratigraphy, Nanjing Institute of Geology and Palaeontology, Chinese Academy of Sciences, Nanjing, China. Micro-drilled sample digestion was performed through sodium hydroxide fusion in a silver crucible with a low flux-to-sample mass ratio of 5 : 1, utilizing electronic grade NaOH (Sigma-Aldrich semiconductor grade) to maintain ultralow procedural blanks. Boron purification was achieved through ion-exchange chromatography using Amberlite® IRA-743 B-specific resin, with targeted B elution in 0.6 mL of 3% HNO_3. Finally, solution B isotope analysis was conducted on a Neptune Plus MC-ICP-MS (Thermo Fisher), where L3 and H3 Faraday cups were used to collect ^{10}B and ^{11}B isotopes, respectively. Total procedural blanks remained below 2 ng throughout both ion-exchange chromatography and MC-ICP-MS analytical sequences, demonstrating exceptional background control. Mass bias correction was achieved through the SSB method with NIST SRM 951a as the primary reference standard, which has an identical B isotopic composition to commonly used NIST SRM 951.[49] The B isotope results were expressed as a per mil deviation relative to NIST SRM 951a:

$$\delta^{11}B_{\text{sample}} = [(^{11}B/^{10}B)_{\text{sample}}/(^{11}B/^{10}B)_{\text{SRM 951a}} - 1] \times 1000 \quad (1)$$

The monitor standard seawater yielded a mean $\delta^{11}B$ of 39.68 ± 0.20‰ ($n = 3$, 2SD), agreeing well with its reported values of 39.61 ± 0.20‰ (2SD).[50] The analytical approach was similar to that outlined by Li *et al.*[51]

2.4 LA-MC-ICP-MS B isotope analysis

In situ tourmaline B isotopic compositions were determined with an NWRFemtoUC Dualwave femtosecond laser ablation system (ESL, USA) connected to a Neptune Plus MC-ICP-MS (Thermo Fisher) at the SKLCEL. The pharos laser is equipped with a fundamental near-infrared wavelength (1028 nm), which produces a 257 nm ultraviolet (UV) laser at the fourth harmonic and 206 nm UV laser at the fifth harmonic with a pulse width of 190 fs. The Neptune Plus was operated in medium-resolution mode. The L3 and H3 Faraday cups were configured for simultaneous detection of ^{10}B and ^{11}B isotopes, respectively. Each analysis includes 100 cycles, with an integration time of 0.524 s per cycle. For all samples, line-scan mode ablation was performed, with a line length of approximately 120 μm, using a line scanning speed of 2 μm s^{-1}, a laser spot size of 45 μm, a repetition rate of 20 Hz, and an energy density of ~1.2 J cm^{-2}. Each time-resolved analysis dataset includes approximately 30 s of blank signal, 60 s of sample signal, and 50 s of washout. For comparison, a 193 nm ArF excimer laser with a pulse width of 20 ns (RESOLution S155-LR, ASI) connected to a Nu Plasma 1700 MC-ICP-MS (Nu instrument, UK) was also used to determine the B isotopic compositions. Cup configurations for B isotope detection were the L6 Faraday cup for ^{10}B and H3 cup for ^{11}B. Each analysis includes 250 cycles, with an integration time of 0.2 s per cycle. All measurements were carried out in a single-spot ablation mode with laser spot sizes of 67 μm, a repetition rate of 8 Hz, and an energy density of ~4 J cm^{-2}. Each time-resolved analysis dataset includes approximately 30 s of blank signal, 60 s of sample signal, and 60 s of washout. The SSB method was used to calibrate the mass bias of the instrument. The detailed instrumental settings of the LA-MC-ICP-MS are listed in Table 1.

Another set of *in situ* B isotopic composition measurements of tourmalines was performed on a Neptune Plus MC-ICP-MS (Thermo Fisher Scientific, Germany) equipped with a 193 nm ArF laser ablation system (GeoLas Pro, Coherent, Germany) at the Key Laboratory for the Study of Focused Magmatism and Giant Ore Deposits, Xi'an Center of China Geological Survey (XCCGS). The SSB method was employed to correct the IMF. A series of reference materials schorl HS#112566, dravite HS#108796, and elbaite HS#98144 were used as the bracketing standards for TOUR1–TOUR4, TOUR5, and TOUR6, respectively.

Table 1 Operating parameters for B isotope measurements during LA-MC-ICP-MS

MC-ICP-MS	Neptune Plus	Nu Plasma 1700
RF power	1200 W	1300 W
Cooling gas	15 L min^{-1}	13 L min^{-1}
Auxiliary gas	0.8 L min^{-1}	0.8 L min^{-1}
Cycle number	100	250
Integration time	0.524 s	0.2 s
Laser ablation system	NWR-FemtoUC	RESOLution S155-LR
Wavelength	257 nm	193 nm
Pulse duration	190 fs	20 ns
Energy density	~1.2 J cm^{-2}	~4 J cm^{-2}
Frequency	20 Hz	8 Hz
Carrier gas	400 mL min^{-1}	280 mL min^{-1}
Ablation mode	Line scan	Single spot
Spot size	45 μm	67 μm

The LA-MC-ICP-MS analysis of B isotopes was conducted at Key Laboratory of Mineral Resources in Western China, Lanzhou University, China (LZU). The experiment was carried out with a 193 nm ArF laser system (RESOLution S155-LR, ASI) combined with a Nu Plasma II MC-ICP-MS (Nu instrument, UK) using the SSB method. GIGT was used as the bracketing standard for TOUR5 and the self-calibrated method was used for TOUR1, TOUR4, and TOUR6.

3. Results and discussion

3.1 Major element determination

The major element contents are summarized in Table 2. The geochemical analyses reveal distinct compositional variations among the tourmaline samples. In these tourmalines, SiO_2 and Al_2O_3 constitute the most abundant compounds, with contents ranging from 34.6 wt% to 37.6 wt% for SiO_2 and 29.5 wt% to 39.4 wt% for Al_2O_3. TOUR1 and TOUR4 exhibit significantly elevated FeO concentrations (17.1 wt% and 16.0 wt%, respectively), in contrast to the low FeO contents observed in TOUR2, TOUR3, TOUR5, and TOUR6 (0.24–2.82 wt%). Conversely, TOUR2, TOUR3, and TOUR5 are characterized by high MgO levels (9.24–10.4 wt%), while TOUR1, TOUR4, and TOUR6 show markedly lower MgO concentrations (0.00–1.09 wt%). TOUR6 tourmaline are characterized by higher Al_2O_3 (39.4 ± 0.75 wt%) than other tourmalines (29.5–33.1 wt%). As shown in Fig. 2, classification following Henry *et al.*[52] demonstrates that all tourmaline samples belong to the alkalic group based on *X*-site occupancy (Fig. 2a). Subgroup discrimination by *Y*-site occupancy reveals three distinct populations: TOUR1 and TOUR4 plot within the schorl field and TOUR2, TOUR3, and TOUR5 plot in the dravite field, while TOUR6 is classified as elbaite (Fig. 2b). This suggests three different geochemical groups within these tourmalines.

3.2 SN-MC-ICP-MS for the bulk B isotope measurement results

The B isotopic compositions of the six tourmaline samples were determined by SN-MC-ICP-MS and the $\delta^{11}B$ values relative to NIST SRM 951a are shown in Table 3. For schorl, the $\delta^{11}B$ values of TOUR1 and TOUR4 are −11.26 ± 0.06‰ (2SE) and −13.31 ± 0.07‰ (2SE), respectively. For dravite, three samples yielded −11.82 ± 0.05‰ (2SE), −11.33 ± 0.06‰ (2SE), and −8.88 ± 0.05‰ (2SE) for TOUR2, TOUR3, and TOUR5, respectively. The elbaite TOUR6 yields a $\delta^{11}B$ value of −8.57 ± 0.04‰ (2SE).

3.3 Assessment of matrix effects by fs-LA and ns-LA

Matrix effects in the laser ablation analysis process result in inaccurate or imprecise isotopic composition measurements. Research has shown that fs-LA generates smaller aerosol particles with a narrow size distribution, shorter laser–matter interaction time, faster heat diffusion, and smaller heat-affected zone compared to ns-LA, significantly reducing the matrix-dependent fractionation effects.[38–41] Based on this basic

Table 2 Major element compositions of the TOUR1-6 tourmalines[a]

	TOUR1		TOUR2		TOUR3		TOUR4		TOUR5		TOUR6	
	$n = 23$		$n = 24$		$n = 38$		$n = 29$		$n = 44$		$n = 24$	
Comment	% m/m	1s	% m/m	1s	% m/m	1s	% m/m	1s	% m/m	1s	% m/m	1s
K_2O	0.04	0.02	0.02	0.01	0.01	0.01	0.05	0.03	0.01	0.01	0.02	0.01
CaO	0.07	0.02	1.09	0.23	0.92	0.04	0.06	0.03	0.27	0.03	0.26	0.08
Cr_2O_3	0.02	0.03	0.05	0.04	0.01	0.02	0.01	0.01	0.02	0.02	0.01	0.02
MgO	0.83	0.04	9.87	0.27	9.24	0.17	1.09	0.25	10.4	0.17	0.00	0.00
SiO_2	35.0	0.72	36.1	0.52	36.6	0.46	34.6	0.56	37.6	0.95	36.8	0.72
Na_2O	2.17	0.09	2.07	0.16	2.02	0.08	2.21	0.15	2.46	0.07	2.03	0.13
Al_2O_3	29.5	0.69	32.5	0.44	32.7	0.44	30.7	0.74	33.1	0.29	39.4	0.75
FeO	17.1	0.18	1.09	0.21	2.82	0.13	16.0	0.52	0.24	0.04	1.78	0.87
MnO	0.13	0.03	0.01	0.02	0.01	0.02	0.18	0.03	0.01	0.02	0.45	0.09
TiO_2	0.26	0.04	0.60	0.12	0.52	0.06	0.38	0.12	0.41	0.06	0.01	0.05
B_2O_3[a]	10.0	0.20	10.6	0.10	10.7	0.12	10.0	0.11	10.9	0.19	10.7	0.14
Li_2O[a]	0.29	0.07	0.34	0.04	0.25	0.03	0.15	0.09	0.35	0.08	1.85	0.12
Total	95.4	1.76	94.3	0.87	95.9	1.05	95.4	0.74	95.7	1.56	93.4	1.02

[a] The calculation method for B_2O_3 and Li_2O can be found in Selway *et al.*[54]

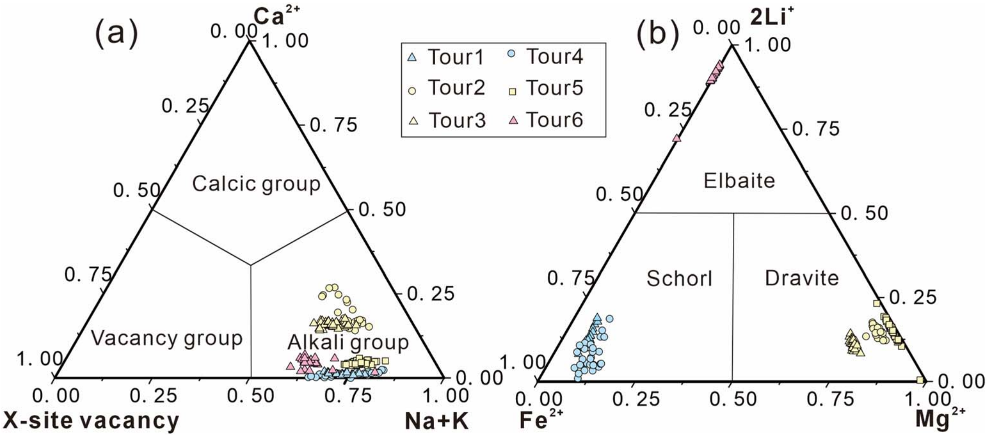

Fig. 2 Classification diagrams of the studied tourmalines following the approach by Henry *et al.*:[52] (a) classification of primary tourmaline groups based on *X*-site occupancy; (b) classification of tourmaline types based on *Y*-site occupancy.

Table 3 B isotopic compositions of the studied tourmalines measured by SN-MC-ICP-MS, fs-LA-MC-ICP-MS, and ns-LA-MC-ICP-MS[a]

	SN-MC-ICP-MS		GIGT as the bracketing standard by fs-LA				GIGT as the bracketing standard by ns-LA			
Sample	$\delta^{11}B$	2SE	$\delta^{11}B$	2SD	Offset	n	$\delta^{11}B$	2SD	Offset	n
Non matrix-matched calibration										
TOUR1	−11.26	0.06	−11.67	0.15	−0.41	30	−11.83	0.42	−0.57	30
TOUR4	−13.31	0.07	−14.01	0.33	−0.70	30	−13.94	0.60	−0.63	30
TOUR6	−8.57	0.04	−9.24	0.45	−0.67	30	−9.20	0.45	−0.63	30
Matrix-matched calibration										
TOUR2	−11.82	0.05	−12.03	1.12	−0.21	30	−11.70	1.18	0.12	30
TOUR3	−11.33	0.06	−11.55	0.39	−0.22	30	−11.62	0.55	−0.29	30
TOUR5	−8.88	0.05	−9.06	0.40	−0.18	30	−9.32	0.54	−0.44	30
	SN-MC-ICP-MS		TOUR1 as the bracketing standard by fs-LA				TOUR1 as the bracketing standard by ns-LA			
TOUR6	−8.57	0.04	−9.48	0.21	−0.91	30	−9.13	0.38	−0.56	30

[a] Offset represents the deviation between $\delta^{11}B$ values of LA-MC-ICP-MS and $\delta^{11}B$ values of SN-MC-ICP-MS.

principle, the matrix effects during fs-LA and ns-LA analyses were systematically evaluated by measuring B isotopic compositions across a series of chemically diverse tourmalines, including schorl, elbaite, and dravite. The results are summarized in Table 3 and Fig. 3.

3.3.1 Non-matrix-matched calibration of B isotope analysis. We employed a non-matrix-matched calibration strategy, where B isotopic compositions in two schorl (TOUR1 and TOUR4) samples and one elbaite (TOUR6) sample were standardized against a dravite sample (GIGT[48]) as a bracketing standard to correct for instrumental mass bias. Three tourmalines were repeatedly analyzed thirty times by fs-LA and ns-LA, and their δ^{11}B values were compared with the SN-MC-ICP-MS values obtained using micro-drilling. For ns-LA, using dravite GIGT as a bracketing standard to analyze TOUR1, TOUR4, and TOUR6 yielded inaccurate δ^{11}B values of $-11.83 \pm 0.42‰$, $-13.94 \pm 0.60‰$ and $-9.20 \pm 0.45‰$, respectively. These measurements consistently deviated negatively by $-0.63‰$ to $-0.57‰$ from solution values, indicating that the dravite (GIGT) is unsuitable as a calibrating RM for schorl and elbaite due to significant matrix effects. In addition, when using TOUR1 as the bracketing standard for TOUR6 analysis, the measured δ^{11}B value of $-9.13 \pm 0.38‰$ exhibits a systematic negative offset of $-0.56‰$ relative to the SN-MC-ICP-MS value. This deviation highlights the significant matrix mismatch between schorl TOUR1 and elbaite TOUR6, resulting in a large bias in B isotopic composition measurements.

Similarly, fs-LA analyses using GIGT as a bracketing standard yielded δ^{11}B values of $-11.67 \pm 0.15‰$, $-14.01 \pm 0.33‰$ and $-9.24 \pm 0.45‰$ for TOUR1, TOUR 4, and TOUR6, respectively, exhibiting larger negative deviations spanning from $-0.70‰$ to $-0.41‰$ relative to solution values. In addition, the δ^{11}B values of TOUR6, calibrated using TOUR1 as the bracketing standard, yielded a value of $-9.48 \pm 0.21‰$, showing a large deviation of $-0.91‰$ from the SN-MC-ICP-MS value. A previous study has reported matrix effects on B isotopic compositions across different types of tourmalines. Chaussidon and Albarède[26] found that variations in chemical composition of tourmaline (occupation of the X site and the Li content) can affect the IMF and that Li-rich tourmaline is richer in ^{11}B compared to Fe and/or Mg-rich tourmaline. And Liao *et al.*[47] obtained δ^{11}B values of $-6.18 \pm 0.56‰$ for dravite HM108796 using the schorl MD-B66 as the bracketing standard by ns-LA-MC-ICP-MS, with a deviation of 0.68‰ compared to literature values.

Our results show that using dravite (GIGT) as a bracketing standard to determine boron isotopes in schorl (TOUR1 and TOUR 4) and elbaite (TOUR6) with either 257 nm UV-fs-LA-MC-ICP-MS or 193 nm UV-ns-LA-MC-ICP-MS suffers from severe matrix effects, leading to systematic deviations of up to $-0.70‰$ for fs-LA and $-0.63‰$ for ns-LA in non-matrix-matched calibrations. Notably, this phenomenon aligns with findings by Zheng *et al.*,[40] who found that inaccurate and imprecise ^{56}Fe/^{54}Fe ratios were obtained when magnetite and pyrrhotite were analyzed against non-matrix matched standards (pyrite or Fe metal). They attributed these inaccuracies to matrix effects caused by the compositional differences between samples and standards, influencing space-charge effects in ICP-MS. Similarly, Ikehata and Hirata[53] found the δ^{65}Cu shifts over 0.76‰ for cubanite calibrated against pure copper NIST SRM 976 using 206 nm UV-fs-LA-MC-ICP-MS. All these observed deviations in boron isotopic composition analysis necessitate matrix-matched calibration protocols to ensure high precision and accuracy of *in situ* boron isotope analysis.

3.3.2 Matrix-matched calibration of B isotope analysis. Then we utilized a matrix-matched calibration strategy in analyzing three types of tourmalines. For dravite, laser ablation analyses using GIGT as the bracketing standard yielded δ^{11}B values of $-12.03 \pm 1.12‰$, $-11.55 \pm 0.39‰$, and $-9.06 \pm 0.40‰$ for TOUR2, TOUR3, and TOUR5 with fs-LA and $-11.70 \pm 1.18‰$, $-11.62 \pm 0.55‰$, and $-9.32 \pm 0.54‰$ with ns-LA, respectively. Both calibrated results are consistent with the SN-MC-ICP-MS values within the analytical uncertainty of $-0.44‰$ to 0.12‰. For schorl, these two tourmalines mutually corrected the boron isotopic compositions. The δ^{11}B value of TOUR1 was $-11.05 \pm 0.41‰$ using TOUR4 as the bracketing standard (Fig. 5a), consistent with the solution result within an uncertainty of 0.21‰. Conversely, using TOUR1 as the bracketing standard, the TOUR4 produced a δ^{11}B value of $-13.51 \pm 0.44‰$ (Fig. 5b), which aligns with the solution results within 0.20‰ uncertainty. For elbaite without an available certified RM, a self-bracketing SSB method was implemented for TOUR6. The obtained δ^{11}B value of $-8.57 \pm 0.17‰$ perfectly aligns with the SN-MC-ICP-MS result ($\Delta_{\text{LA}-\text{SN}} = 0.00‰$), validating the accuracy and necessity of matrix-matched calibration. Therefore, obtaining reliable boron isotopic compositions necessitates calibration against matrix-matched RMs.

3.4 B isotopic compositions of schorl, elbaite and dravite

Due to the lack of matrix-matched RMs, a self-calibrated method using the SSB approach was selected to correct the instrument mass bias for schorl (TOUR1 and TOUR4) using LA-MC-ICP-MS. A total of 257 measurements on TOUR1 yielded a grand mean δ^{11}B of $-11.25 \pm 0.24‰$ (2SD), demonstrating excellent consistency with the solution MC-ICP-MS results within analytical error (Fig. 4a). Similarly, all 174 δ^{11}B measurements on TOUR4 yielded a mean value of $-13.24 \pm 0.64‰$ (2SD), agreeing with the SN-MC-ICP-MS data (Fig. 4d). These results indicate the B isotopic compositions of the two schorl samples are homogeneous at least on a scale of tens of micrometers. To further assess the B isotope homogeneity of TOUR1 and TOUR4, cross-calibration experiments were conducted, with TOUR1 and TOUR4 serving as mutual bracketing RMs. A total of 340 δ^{11}B analyses of TOUR1 and 335 analyses of TOUR4 yielded a mean value of $-11.05 \pm 0.41‰$ (2SD) and $-13.51 \pm 0.44‰$ (2SD), respectively (Fig. 5a and b). Additionally, a total of 597 spots on TOUR1 and 509 spots on TOUR4 analyzed for B isotopes by LA-MC-ICP-MS both show a Gaussian distribution (Fig. 6a and b). Repeated analyses of TOUR1 and TOUR4 demonstrate excellent external reproducibility, with a value of $-11.14 \pm 0.40‰$ (2SD, $n = 597$) for TOUR1 and $-13.42 \pm 0.57‰$ (2SD, $n = 509$) for TOUR4. These findings confirm that the homogeneous distribution of B isotopes satisfies the essential

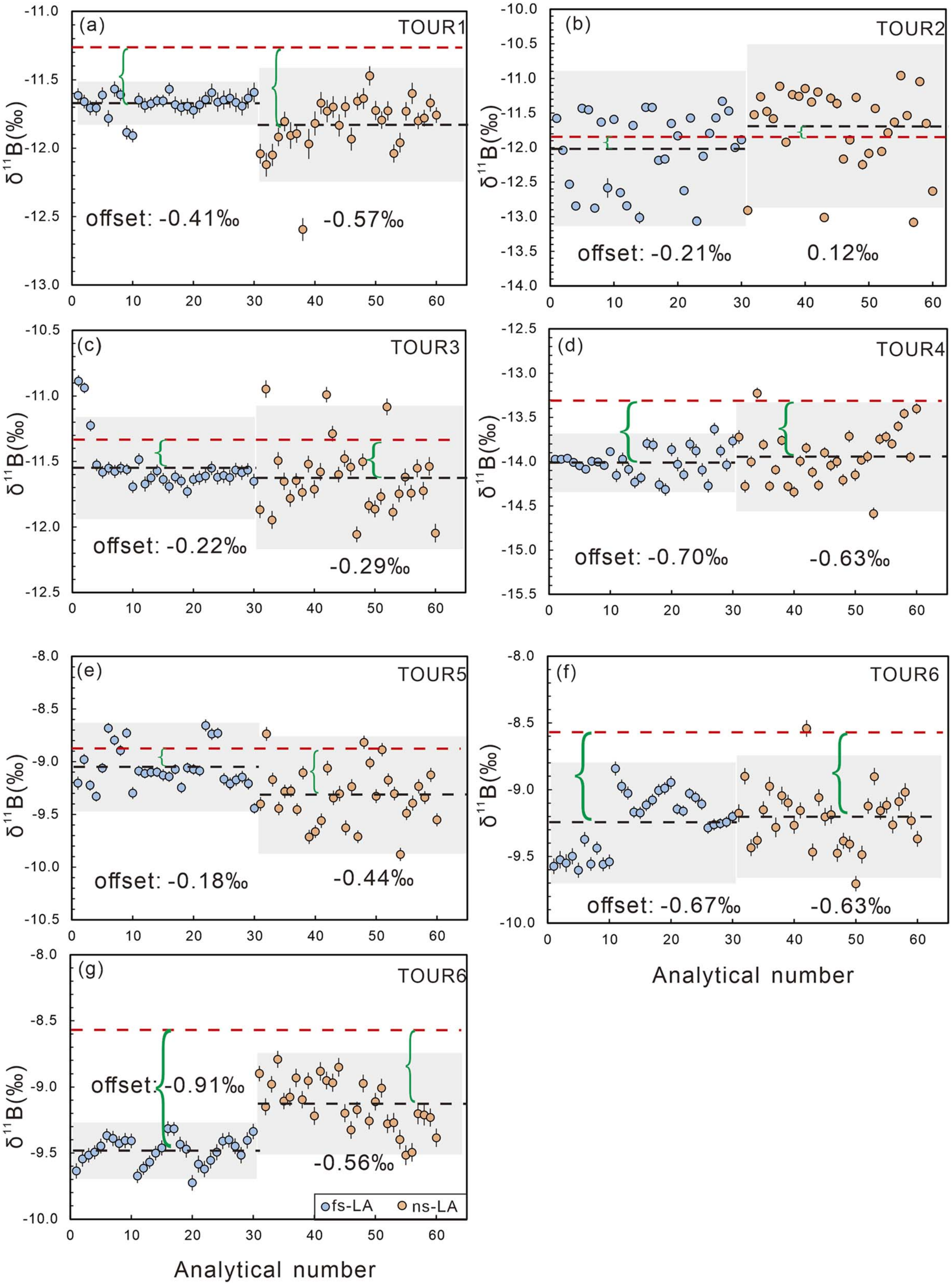

Fig. 3 Comparison of δ^{11}B values between femtosecond laser ablation and nanosecond laser ablation. The red and black dashed lines represent the SN-MC-ICP-MS and LA-MC-ICP-MS values, respectively. Error bars for a single analysis are 2SE, and the gray areas represent 2SD of each measured sample. (a–f) GIGT as the bracketing standard. (g) TOUR1 as the bracketing standard. Offset represents the deviation of δ^{11}B values relative to the SN-MC-ICP-MS value.

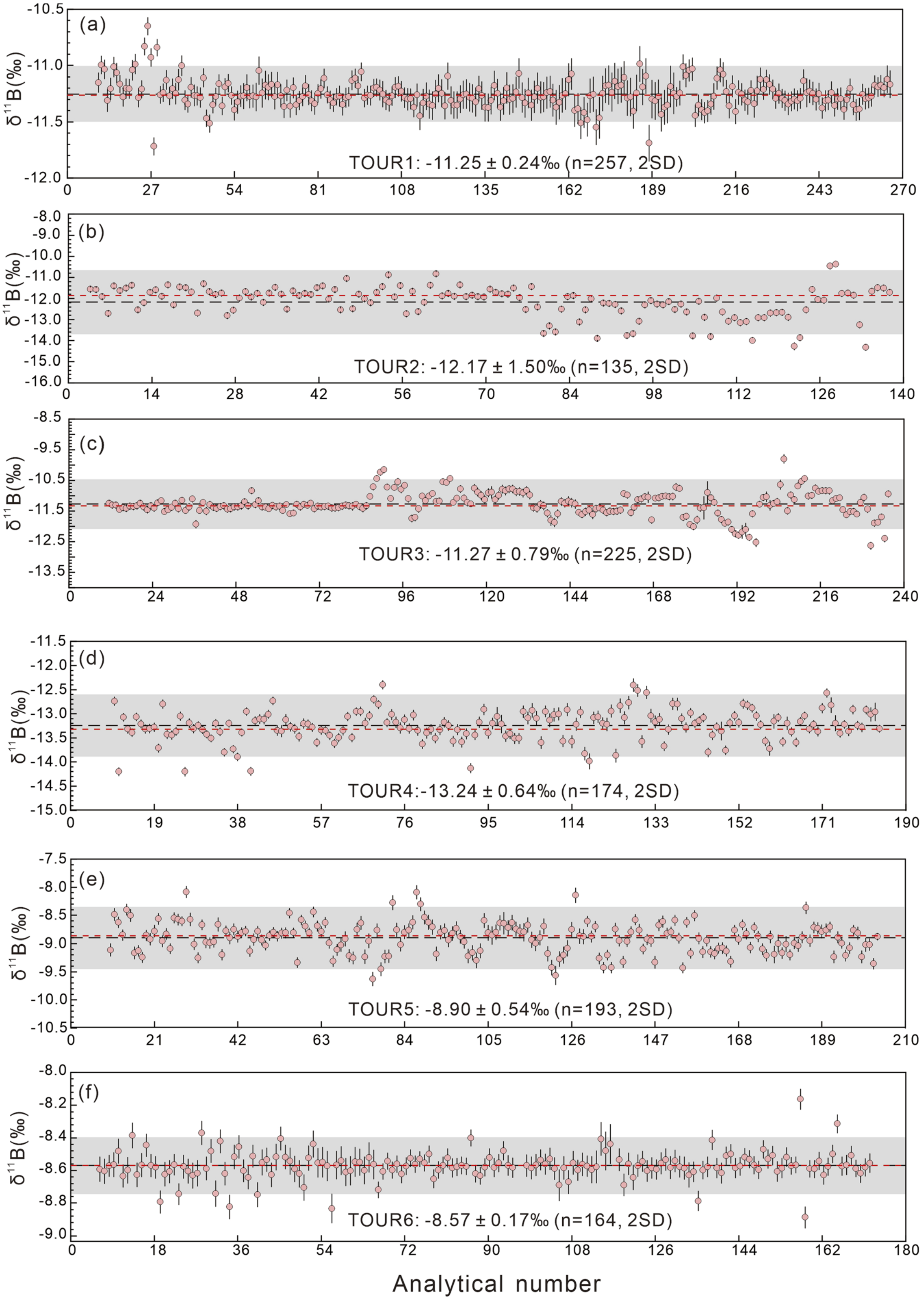

Fig. 4 δ^{11}B values measured by LA-MC-ICP-MS for (a) TOUR1, (b) TOUR2, (c) TOUR3, (d) TOUR4, (e) TOUR5, and (f) TOUR6 with the self-calibrated method. The red and black dashed lines represent the SN-MC-ICP-MS and LA-MC-ICP-MS values, respectively. The error bars represent 2SE for a single analysis, and the gray areas represent 2SD of each measured sample.

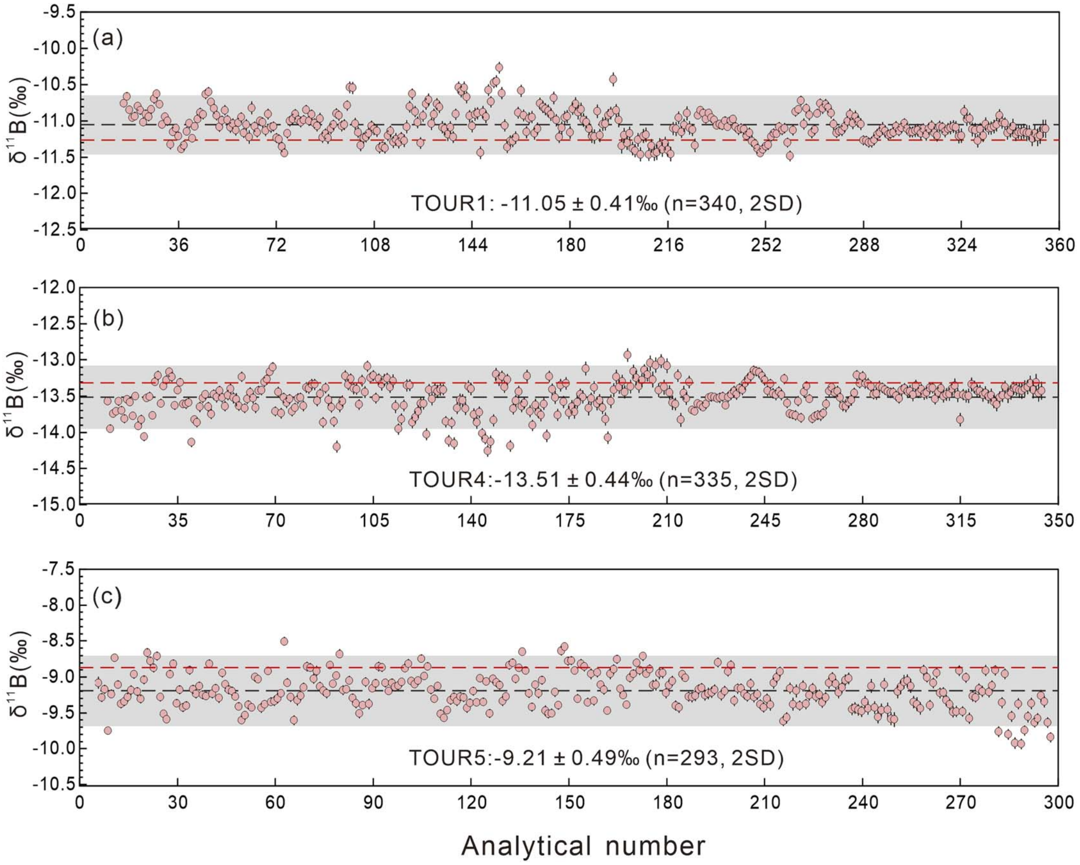

Fig. 5 δ^{11}B values measured by LA-MC-ICP-MS for (a) TOUR1, (b) TOUR4, and (c) TOUR5 with GIGT as the bracketing standard. The red and black dashed lines represent the SN-MC-ICP-MS and LA-MC-ICP-MS values, respectively. Error bars represent 2SE for a single analysis, and the gray areas represent 2SD of each measured sample.

requirements for reliable *in situ* B isotope analysis in schorl using LA-MC-ICP-MS.

For dravite TOUR5, two calibration methods were applied to evaluate its B isotope homogeneity. The first method utilized a matrix-matched standard (GIGT) to calibrate the B isotope ratios, yielding a mean δ^{11}B value of $-9.21 \pm 0.49‰$ (2SD) from 293 analyses (Fig. 5c). The second calibration method employed the self-calibrated SSB approach, with 193 measurements giving a mean δ^{11}B value of $-8.90 \pm 0.54‰$ (2SD) (Fig. 4e). The δ^{11}B values of TOUR5 obtained through the two calibration methods are consistent with the results obtained *via* SN-MC-ICP-MS within uncertainty. Besides, a total of 486 spots analyzed for TOUR5 formed a Gaussian distribution (Fig. 6c) with a grand mean value of $-9.09 \pm 0.60‰$ (2SD). In contrast, analyses of dravite TOUR2 (δ^{11}B $= -12.17 \pm 1.50‰$, $n = 135$) and TOUR3 (δ^{11}B $= -11.27 \pm 0.79‰$, $n = 225$) using the self-calibrated method show significantly heterogeneous distribution in B isotope ratios (Fig. 4b and c).

For elbaite TOUR6, all 164 δ^{11}B ratios follow the Gaussian distribution (Fig. 6d), yielding a grand mean value of $-8.57 \pm 0.17‰$ (2SD) by LA-MC-ICP-MS using the self-calibrated SSB calibration approach, agreeing well with the SN-MC-ICP-MS results within analytical uncertainty (Fig. 4f). Therefore, we can preliminarily conclude that, given the current accuracy of

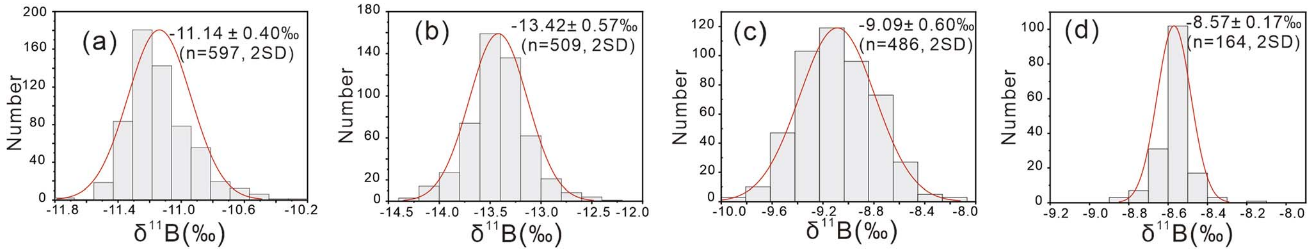

Fig. 6 Frequency histograms and probability density curves of δ^{11}B values for (a) TOUR1; (b) TOUR4; (c) TOUR5; (d) TOUR6.

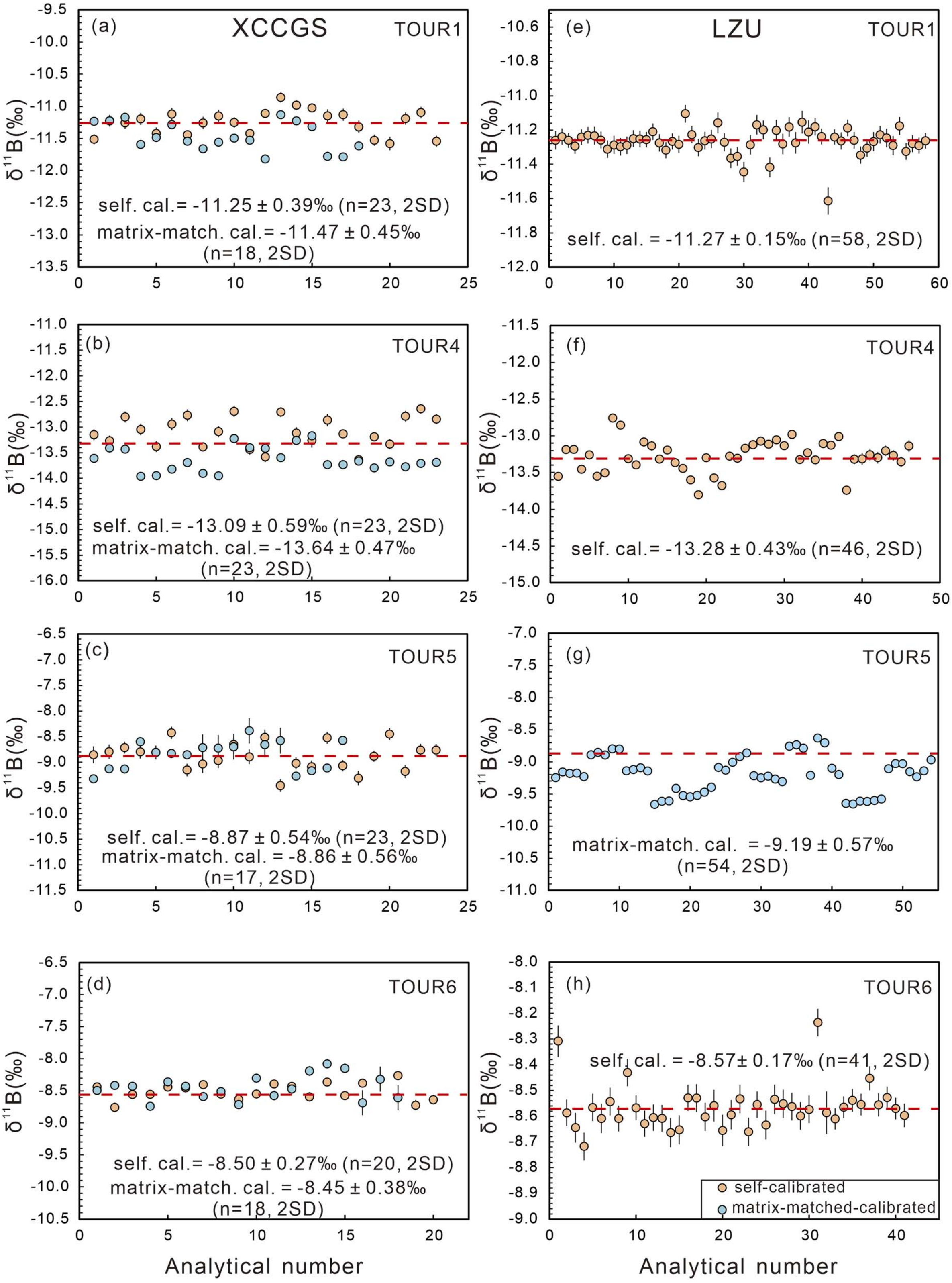

Fig. 7 δ^{11}B values of TOUR1, TOUR4, TOUR5 and TOUR6 measurement by LA-MC-ICP-MS in XCCGS (a–d), LZU (e–h). The red dashed lines represent the SN-MC-ICP-MS values. Error bars are the 2SE for a single analysis. XCCGS: Key Laboratory for the Study of Focused Magmatism and Giant Ore Deposits, Xi'an Center of China Geological Survey; LZU: Key Laboratory of Mineral Resources in Western China, Lanzhou University, China.

Table 4 Results of δ^{11}B values (mean ± 2s) in reference materials

	In situ δ^{11}B by LA-MC-ICP-MS	BuIk δ^{11}B by TIMS/MC-ICP-MS	
IAEA-B4	−8.60 ± 0.38‰ (*n* = 60)[47]	−8.71 ± 0.18‰[43]	
Schorl HS#112566	−13.36 ± 0.57‰ (*n* = 58)[47]	−13.86 ± 0.36‰[31]	
	−13.66 ± 0.48‰ (*n* = 11) RM: TOUT1 (in this study)		
	−13.42 ± 0.42‰ (*n* = 10) RM: TOUT4 (in this study)		
Dravite HS#108796	−6.18 ± 0.56‰ (*n* = 59)[47]	−6.6 ± 0.10‰[44]	
	−6.10 ± 0.62‰ (*n* = 6) (in this study)		
Elbaite HS#98144	−11.91 ± 0.57‰ (*n* = 58)[47]	−10.5 ± 0.20‰[44]	
	−10.51 ± 0.55‰ (*n* = 6) (in this study)		
IMR RB1	−13.05 ± 0.54‰ (*n* = 41)[47]	−12.22 ± 1.10‰[37]	
	−12.96 ± 0.97‰ (*n* = 57)[37]		
IMR RB2	−12.53 ± 0.57‰ (*n* = 21)[37]	−12.10 ± 0.78‰[37]	
GIGT	12.63 ± 0.51‰ (*n* = 74)[48]	−12.65 ± 0.12‰[48]	
	−12.31 ± 0.42‰ (*n* = 10) (in this study)		
XJ-1	−11.90 ± 0.64‰ (*n* = 78)[48]	−11.90 ± 0.24‰[48]	
XJ-3	−11.91 ± 0.64‰ (*n* = 73)[48]	−11.89 ± 0.19‰[48]	
MD-B66	−7.74 ± 0.25‰ (*n* = 251)[47]	−7.71 ± 0.32‰[47]	
IM-B232	−13.27 ± 0.48‰ (*n* = 80)[47]	−13.17 ± 0.62‰[47]	
BR-DG68	−14.02 ± 0.61‰ (*n* = 112)[47]	−13.85 ± 0.32‰[47]	
HGL-3	−12.38 ± 0.38‰ (*n* = 485)[46]	−12.56 ± 0.24‰[46]	
TOUR1	**−11.25 ± 0.24‰ (*n* = 257)**	**−11.26 ± 0.06‰**	**New RMs in this study**
TOUR4	**−13.24 ± 0.64‰ (*n* = 174)**	**−13.31 ± 0.07‰**	
TPUR5	**−8.90 ± 0.54‰ (*n* = 193)**	**−8.88 ± 0.05‰**	
TOUR6	**−8.57 ± 0.17‰ (*n* = 164)**	**−8.57 ± 0.04‰**	

LA-MC-ICP-MS analysis, the B isotopic compositions of TOUR1, TOUR4, TOUR5, and TOUR6 tourmalines are sufficiently uniform at scales greater than tens of micrometers.

3.5 Reliability of *in situ* δ^{11}B values

To evaluate the reliability of *in situ* δ^{11}B values in these reference materials, the B isotope ratios for TOUR1, TOUR4, TOUR5, and TOUR6 were analyzed using LA-MC-ICP-MS at two other laboratories: XCCGS and LZU. The inter-laboratory comparison results are summarized in Fig. 7. At XCCGS, the *in situ* analysis yielded a mean δ^{11}B value of −11.25 ± 0.39‰ (2SD, $n = 23$) and −11.47 ± 0.45‰ (2SD, $n = 18$) for TOUR1, −13.09 ± 0.59‰ (2SD, $n = 23$) and −13.64 ± 0.47‰ (2SD, $n = 23$) for TOUR4, −8.87 ± 0.54‰ (2SD, $n = 23$) and −8.86 ± 0.56‰ (2SD, $n = 17$) for TOUR5, and −8.50 ± 0.27‰ (2SD, $n = 20$) and −8.45 ± 0.38‰ (2SD, $n = 18$) for TOUR6, with self-calibration and matrix-matched calibration, respectively. At LZU, the *in situ* analysis yielded a mean δ^{11}B value of −11.27 ± 0.15‰ (2SD, $n = 58$) for TOUR1, −13.28 ± 0.43‰ (2SD, $n = 46$) for TOUR4, and −8.57 ± 0.17‰ (2SD, $n = 41$) for TOUR6 with the self-calibrated method. TOUR5 yielded a mean value of −9.19 ± 0.57‰ (2SD, $n = 54$) with GIGT as the bracketing standard. All δ^{11}B values from different laboratories are consistent and also agree well with the *in situ* results determined in our laboratory. And the LA-MC-ICP-MS results are identical to those obtained by SN-MC-ICP-MS within uncertainties.

Furthermore, some fragments of TOUR1–TOUR4, TOUR5, and TOUR6 were used as matrix-matched RMs for bracketing standards to calibrate the schorl HS#112566, dravite HS#108796, and elbaite HS#98144, respectively. The results are listed in Table 4. Repeated measurements by LA-MC-ICP-MS yielded δ^{11}B values of −13.66 ± 0.48‰ (2SD, $n = 11$) with TOUR1 as the bracketing standard, −13.42 ± 0.42‰ (2SD, $n = 10$) with TOUR4 as the bracketing standard for schorl HS#112566, −6.10 ± 0.62‰ (2SD, $n = 6$) for dravite HS#108796, and −10.51 ± 0.55‰ (2SD, $n = 6$) for elbaite HS#98144, which all agree with their corresponding δ^{11}B values with SN-MC-ICP-MS within the uncertainty range. These results reflect the relatively good reliability of the LA-MC-ICP-MS analysis process.

4. Conclusion

The boron isotopic compositions of chemically diverse tourmalines were analyzed using both 257 nm femtosecond and 193 nm nanosecond laser ablation systems coupled with MC-ICP-MS. Matrix-matched RMs are required because matrix effects result in significant δ^{11}B deviations of up to −0.70‰ (fs-LA) and −0.63‰ (ns-LA) when calibrating elbaite against the dravite (GIGT) reference material. These findings highlight the critical role of matrix-matched standards in achieving accurate δ^{11}B determinations in chemically diverse tourmalines.

Furthermore, a series of Fe-, Mg-, and Li-rich tourmaline samples was systematically characterized for boron isotope analysis *via* LA-MC-ICP-MS. Their homogeneous isotopic compositions and high measurement precisions demonstrate that TOUR1, TOUR4, TOUR5, and TOUR6 are highly suitable as matrix-matched calibration standards for isotope calibration, quality control, and method validation *in situ* boron isotope analysis. The mean δ^{11}B values obtained using LA-MC-ICP-MS agree well with SN-MC-ICP-MS values within the 2SD analytical uncertainty, and thus we recommend the following δ^{11}B values obtained *via* SN-MC-ICP-MS for RMs: −11.26 ± 0.06‰ for TOUR1, −13.31 ± 0.07‰ for TOUR4, −8.88 ± 0.05‰ for TOUR5, and −8.57 ± 0.04‰ for TOUR6, with uncertainties reported as 2SE.

Data availability

The authors declare that the data supporting the findings of this study are available within the paper and its ESI files.† Should any raw data files be needed in another format they are available from the corresponding author upon reasonable request. Source data are provided with this paper.

Author contributions

Xiaojuan Nie and Yan Zhang performed the experiments and wrote the draft of the manuscript. Zhian Bao designed the experiment and interpreted the data. Honglin Yuan led the project and conceived the study. Kaiyun Chen provided suggestions for this experiment. Wenqiang Yang performed the EPMA analyses. All co-authors contributed to the paper writing.

Conflicts of interest

The authors declare that they have no conflict of interest.

Acknowledgements

We thank two anonymous reviewers for their insightful and helpful comments. We thank Le Zhang from the Guangzhou Institute of Geochemistry, Chinese Academy of Sciences for providing the GIGT tourmaline. We thank Shuangshuang Wang from the Xi'an Center of China Geological Survey for the LA-MC-ICP-MS analysis. We thank Xiuhong Liao from the China University of Geosciences, Wuhan, for help with classification of tourmaline types. This work was supported by grants awarded by the National Natural Science Foundation of China (Grants 42130102 and 42173033) and the MOST Special Foundation from the State Key Laboratory of Continental Evolution and Early Life (Northwest University).

References

1 G. L. Foster, C. Lécuyer and H. R. Marschall, in *Encyclopedia of Geochemistry*, ed. W. M. White, Springer, Berlin, 2016, pp. 1–6.
2 B. L. Dutrow and D. J. Henry, *Elements*, 2011, **7**, 301–306.
3 D. J. Henry and B. L. Dutrow, *Lithos*, 2012, **154**, 16–32.
4 D. J. Henry and B. L. Dutrow, *Jour. Geosci.*, 2018, **63**, 77–98.
5 R. Halama, M. Konrad-Schmolke and J. C. M. De Hoog, *Contrib. Mineral. Petrol.*, 2020, **175**, 20.
6 S. Huang, Y. Song, Z. Hou and C. Xue, *Chem. Geol.*, 2016, **439**, 173–188.
7 M.-S. Krienitz, R. B. Trumbull, A. Hellmann, J. Kolb, F. M. Meyer and M. Wiedenbeck, *Miner. Deposita*, 2008, **43**, 421–434.
8 J.-X. Li, W.-M. Fan, L.-Y. Zhang, L. Ding, Y.-H. Yue, J. Xie, F.-L. Cai and K. Sein, *Lithos*, 2020, **356–357**, 105380.
9 T. Shen, H. Hu, L. Zhang, J. D. Xu, Z. Tian, T. Bader, J. Ma, J. Zhang, W. Peng and J. Yang, *J. Petrol.*, 2024, **65**, egae116.
10 V. J. Van Hinsberg, G. Franz and B. J. Wood, *Geochem. Persp. Let.*, 2017, **3**, 160–169.
11 Z. Wang, B. Chen and X. Yan, *Precambrian Res.*, 2019, **326**, 258–271.
12 Q. Zhou, W. Li, G. Wang, Z. Liu, Y. Lai, J. Huang, G. Yan and Q. Zhang, *Lithos*, 2019, **326–327**, 529–539.
13 S. H. Büttner, W. Reid, J. Glodny, M. Wiedenbeck, G. Chuwa, T. Moloto and A. Gucsik, *Precambrian Res.*, 2016, **280**, 161–178.
14 K. Drivenes, R. B. Larsen, A. Müller, B. E. Sørensen, M. Wiedenbeck and M. P. Raanes, *Contrib. Mineral. Petrol.*, 2015, **169**, 56.
15 D. J. Henry and C. V. Guidotti, *Am. Mineral.*, 1985, **70**, 1–15.
16 G. L. Foster, *Earth Planet. Sci. Lett.*, 2008, **271**, 254–266.
17 Q. Tang, L. Chen, S. Tian, W. Hu, Y. Gong and Y. Zi, *Rock Miner. Anal.*, 2024, **43**, 201–212.
18 M.-Y. He, L. Deng, H. Lu and Z.-D. Jin, *J. Anal. At. Spectrom.*, 2019, **34**, 1026–1032.
19 L. Feng, Z. Li, Q. Cao, S. Tian, W. Huang and T. Wang, *Rock Miner. Anal.*, 2023, **42**, 16–38.
20 G. L. Foster, B. Hönisch, G. Paris, G. S. Dwyer, J. W. B. Rae, T. Elliott, J. Gaillardet, N. G. Hemming, P. Louvat and A. Vengosh, *Chem. Geol.*, 2013, **358**, 1–14.
21 J. Trotter, P. Montagna, M. McCulloch, S. Silenzi, S. Reynaud, G. Mortimer, S. Martin, C. Ferrier-Pagès, J.-P. Gattuso and R. Rodolfo-Metalpa, *Earth Planet. Sci. Lett.*, 2011, **303**, 163–173.
22 M. He, Y. Xiao, Z. Jin, Y. Ma, J. Xiao, Y. Zhang, C. Luo and F. Zhang, *Anal. Chem.*, 2013, **85**, 6248–6253.
23 Y. Ye, N. Aizezi, J. Feng, B. Han, X. Li, Z. Su, L. Li and Y. Liu, *Anal. Chem.*, 2025, **97**, 5554–5562.
24 A. Retzmann, S. Faßbender, M. Rosner, M. Von Der Au and J. Vogl, *J. Anal. At. Spectrom.*, 2023, **38**, 2144–2158.
25 M. Chaussidon, F. Robert, D. Mangin, P. Hanon and E. F. Rose, *Geostand. Newslett.*, 2007, **21**, 7–17.
26 M. Chaussidon and F. Albarède, *Earth Planet. Sci. Lett.*, 1992, **108**, 229–241.
27 M. Rosner, M. Wiedenbeck and T. Ludwig, *Geostand. Geoanal. Res.*, 2008, **32**, 27–38.
28 S. A. Kasemann, D. N. Schmidt, J. Bijma and G. L. Foster, *Chem. Geol.*, 2009, **260**, 138–147.
29 H. R. Marschall and B. D. Monteleone, *Geostand. Geoanal. Res.*, 2015, **39**, 31–46.
30 J. MacGregor, E. S. Grew, J. C. M. De Hoog, S. L. Harley, P. M. Kowalski, M. G. Yates and C. J. Carson, *Geochim. Cosmochim. Acta*, 2013, **123**, 261–283.
31 K. Marger, M. Harlaux, A. Rielli, L. P. Baumgartner, A. Dini, B. L. Dutrow and A. Bouvier, *Geostand. Geoanal. Res.*, 2020, **44**, 593–615.
32 D. Evans, A. Gerdes, D. Coenen, H. R. Marschall and W. Müller, *J. Anal. At. Spectrom.*, 2021, **36**, 1607–1617.
33 L. Lin, Z. Hu, L. Yang, W. Zhang, Y. Liu, S. Gao and S. Hu, *Chem. Geol.*, 2014, **386**, 22–30.

34 P. J. Le Roux, S. B. Shirey, L. Benton, E. H. Hauri and T. D. Mock, *Chem. Geol.*, 2004, **203**, 123–138.

35 C. D. Standish, T. B. Chalk, T. L. Babila, J. A. Milton and G. L. Foster, *Rapid Commun. Mass Spectrom.*, 2019, **33**, 959–968.

36 S. H. Büttner, W. Reid, J. Glodny, M. Wiedenbeck, G. Chuwa, T. Moloto and A. Gucsik, *Precambrian Res.*, 2016, **280**, 161–178.

37 K. Hou, Y. Li, Y. Xiao, F. Liu and Y. Tian, *Chin. Sci. Bull.*, 2010, **55**, 3305–3311.

38 B. Fernández, F. Claverie, C. Pécheyran and O. F. X. Donard, *Trac-Trend Anal. Chem.*, 2007, **26**, 951–966.

39 M. E. Shaheen, J. E. Gagnon and B. J. Fryer, *Chem. Geol.*, 2012, **330–331**, 260–273.

40 X.-Y. Zheng, B. L. Beard and C. M. Johnson, *J. Anal. At. Spectrom.*, 2018, **33**, 68–83.

41 Z. Li, Z. Hu, Y. Liu, S. Gao, M. Li, K. Zong, H. Chen and S. Hu, *Chem. Geol.*, 2015, **400**, 11–23.

42 N. Lv, Z. Bao, K. Chen, K. Wu and H. Yuan, *Sci. China Earth Sci.*, 2022, **65**, 2005–2017.

43 S. Tonarini, M. Pennisi, A. Adorni-Braccesi, A. Dini, G. Ferrara, R. Gonfiantini, M. Wiedenbeck and M. Gröning, *Geostand. Newslett.*, 2003, **27**, 21–39.

44 M. D. Dyar, M. Wiedenbeck, D. Robertson, L. R. Cross, J. S. Delaney, K. Ferguson, C. A. Francis, E. S. Grew, C. V. Guidotti, R. L. Hervig, J. M. Hughes, J. Husler, W. Leeman, A. V. McGuire, D. Rhede, H. Rothe, R. L. Paul, I. Richards and M. Yates, *Geostand. Newslett.*, 2001, **25**, 441–463.

45 W. P. Leeman and S. Tonarini, *Geostand. Newslett.*, 2001, **25**, 399–403.

46 J.-C. Xie, D.-C. Zhu, Q. Wang, L.-L. Zhang, W.-T. Xu and T.-R. Zhang, *Atom. Spectrosc.*, 2024, **45**, 490–497.

47 X. Liao, T. Chen, T. Luo, Y. Cai, W. Zhang, Z. Yin and Z. Hu, *Geostand. Geoanal. Res.*, 2024, 12594.

48 Q. Chen, R.-J. Wang, H.-X. Yu, G. Zhu, Y.-Q. Zhang, X.-P. Xia, Z.-Y. Ren and L. Zhang, *J. Anal. At. Spectrom.*, 2024, **39**, 917–924.

49 S. Misra, R. Owen, J. Kerr, M. Greaves and H. Elderfield, *Cosmochim. Acta.*, 2014, **140**, 531–552.

50 G. L. Foster, P. A. E. Pogge Von Strandmann and J. W. B. Rae, *Geochem. Geophys. Geosyst.*, 2010, **11**, 2010GC003201.

51 Z. Li, Y. Cai, H. Wei, Y. Li, W. Zhang and B. Li, *Geol. J. China Univ.*, 2024, **30**, 133–141.

52 D. J. Henry, M. Novak, F. C. Hawthorne, A. Ertl, B. L. Dutrow, P. Uher and F. Pezzotta, *Am. Mineral.*, 2011, **96**, 895–913.

53 K. Ikehata and T. Hirata, *Anal. Sci.*, 2013, **29**, 1213–1217.

54 J. B. Selway, M. Novák, P. Černý and F. C. Hawthorne, *Eur. J. Mineral.*, 1999, **11**, 569–584.